AIAA SciTech Forum
6-10 January 2025, Orlando, FL
AIAA SCITECH 2025 Forum

10.2514/6.2025-2087

Impact of Combustion and Outflow Modeling on Self-Excited Thermoacoustic Instabilities in a Lean Premixed Swirl-Flame

Michael Pries *, Andreas Fiolitakis †, and Peter Gerlinger ‡
DLR, Stuttgart, Baden Württemberg, 70569, Germany

The computation of self-excited thermoacoustic instabilities remains a challenging task. Reasons are manifold as the problem renders itself as a complex interplay of mixing, combustion, hydrodynamic, and acoustic processes inside a combustion device. To capture the relevant effects, an adequate modeling of the aforementioned processes is needed. In this work, an experimentally well characterized lean premixed swirl flame prone to self-excited thermoacoustic instabilities is investigated by means of compressible Large-Eddy-Simulations (LES). The investigation emphasizes the influence of the outflow modeling as well as the reaction mechanism and the closure model for the chemical source on the flow field. Besides the flow field, the influence on the self excited pressure oscillations in terms of frequency and amplitude is also shown. To further the understanding how outflow modeling and the reaction mechanism affect the results of the LES, simplified one dimensional models are introduced, allowing for a clearer interpretation of the computed results.

I. Introduction

The reduction of pollutant emissions in modern gas turbines led to lean premixed combustion chamber concepts. These systems are known to be prone to combustion instabilities [1]. Especially thermoacoustic instabilities may inflict damage to the combustion device due to high pressure oscillations. Experimental evidence emphasizes an influence of hydrogen addition onto thermoacoustic instabilities [2]. Thus, the recent trend to reduce fossil fuels in favor for hydrogen puts thermoacoustic instabilities further into focus. But, despite being a problem during the development of fuel flexible gas turbines, the computation of thermoacoustic instabilities remains a complex and challenging task. For an accurate computation a thorough modeling of the relevant processes including the effects of mixing, combustion, hydrodynamics, and acoustics in the entire device is required. Hence, to obtain a better understanding of the relevant influencing parameters model burners are often considered. One such experimentally investigated model burner featuring a swirl stabilized lean premixed flame is the PRECCINSTA combustor [3–10]. Depending on the operational point, the combustor may exhibit strong self excited thermoacoustic instabilities. Such a thermoacoustic pulsating operational point is obtained for an equivalence ratio of $\phi = 0.7$ at a thermal power of $P_{\text{th}} = 25\,\text{kW}$ operated under technically premixed conditions. For this operational point a detailed experimental study [3–5] showed a pulsating flame, anchored near the bluff body of the burner. The dominant pressure mode observed in these studies occurs at a frequency of $f = 290\,\text{Hz}$. Follow up experiments [10, 11] measured frequencies of $f = 275\,\text{Hz}$ and $f = 284\,\text{Hz}$, which are slightly lower. Furthermore, opposed to [3–5] a detached flame is observed in [10] for the same operational conditions. The main differences between the measurements in [3–5] and [10] are lower acoustic losses in [10] due to the partial application of sheet metal combustion chamber side walls. In addition, this operational point is also studied by means of compressible Large-Eddy-Simulations (LES) [10–19]. Concerning the frequency as well as the flame lift off height from the burner exit, the computational results differ. In some studies, such as [12, 13, 18, 19] the flame position based on the burner exit temperatures shows a good agreement with the experiments of [3–5]. In contrast, the frequency of the dominant mode is not matched. Other studies obtain a very good agreement of the dominant mode frequency [10, 11, 14] whilst the temperature in the vicinity of the burner exit are underestimated indicating a lifted flame as seen in the experiment of [10]. However, the work of [15–17] prove that a good agreement of both, frequency and flame lift off height as compared to the experiments of [3–5] is achievable. Another noticeable peculiarity is related to the outflow modeling of the available numerical studies in literature. Comparing the considered numerical domains it is apparent that studies involving a large outflow plenum at the downstream end of the combustion device often overestimate the dominant pressure mode frequency [12, 18, 19]. In contrast, a good agreement for the dominant

*Research Scientist, Institute of Combustion Technology, Computer Simulation Department
†Research Scientist, Institute of Combustion Technology, Computer Simulation Department
‡Research Scientist, Institute of Combustion Technology, Computer Simulation Department

pressure mode is generally obtained in studies where a numerical outflow boundary is directly applied to the downstream end of the combustion device [10, 11, 13–17]. Further, a variety of different chemical mechanisms and combustion model approaches have been applied in the numerical studies of [10–19] where the influence of the chosen modeling on the solution remains unclear. The focus of this paper is to investigate the thermoacoustic behavior of the swirl flame by means of compressible LES in order to get a better understanding of the influence parameters affecting the flame anchoring as well as the thermoacoustic oscillation cycle. Therefore, different compressible LES are performed. These computations investigate the influence of the outflow boundary condition as well as the reaction mechanism, the combustion modeling, and the model parameters for the turbulent Prandtl and Schmidt numbers.

II. Numerical Method

The spatially filtered balance equations for mass, momentum, energy, and the transport equations for species mass fractions are given by (Einstein notation)

$$\frac{\partial \overline{\rho}}{\partial t} + \frac{\partial \overline{\rho}\,\widetilde{u}_i}{\partial x_i} = 0, \tag{1}$$

$$\frac{\partial \overline{\rho}\,\widetilde{u}_i}{\partial t} + \frac{\partial \overline{\rho}\,\widetilde{u}_i\widetilde{u}_j}{\partial x_j} - \frac{\partial \overline{\tau}_{ij}+\tau_{t,ij}}{\partial x_j} + \frac{\partial \overline{p}}{\partial x_i} = \overline{\rho}\,\widetilde{f}_i, \tag{2}$$

$$\frac{\partial \overline{\rho}\,\widetilde{E}}{\partial t} + \frac{\partial \overline{\rho}\,\widetilde{u}_i\widetilde{E}}{\partial x_i} + \frac{\partial \widetilde{u}_i\,\overline{p}}{\partial x_i} - \frac{\partial \widetilde{u}_j\left(\overline{\tau}_{ij}+\tau_{t,ij}\right)}{\partial x_i} + \frac{\partial \overline{q}_i+q_{t,i}}{\partial x_i} = \overline{\rho}\,\widetilde{u}_i\widetilde{f}_i + \bar{S}_r, \tag{3}$$

$$\frac{\partial \overline{\rho}\,\widetilde{Y}_\alpha}{\partial t} + \frac{\partial \overline{\rho}\,\widetilde{u}_i\widetilde{Y}_\alpha}{\partial x_i} + \frac{\partial \overline{j}_{\alpha i}+j_{t,\alpha i}}{\partial x_i} = \bar{S}_\alpha. \tag{4}$$

In Eqs. (1)-(4), x_i are the spatial coordinates, t the physical time, ρ the density, u_i is the velocity vector, p the pressure, E is the specific total energy, and Y_α the mass fraction for the species α. The viscous stress tensor is defined through τ_{ij}, the vector of the heat flux is given by q_i, and the diffusive mass flux is $j_{\alpha i}$. Radiative and chemical sources are given by S_r and S_α whereas volume forces are denoted by f_i. The specific total energy is defined as the sum of the specific internal energy and the specific kinetic energy. A mixture of thermally perfect gases is assumed where the state equation for an ideal gas applies. Spatially filtered values are denoted by $\overline{(\cdot)}$ whereas a Favre filtered value is denoted by $\widetilde{(\cdot)}$. Due to the filtering, the subgrid-scale stress tensor $\tau_{t,ij}$, the subgrid-scale heat flux $q_{t,i}$, and the subgrid-scale species mass flux $j_{t,\alpha i}$ arise. The models for these terms are outlined in Sec. IV. Equations (1)-(4) are solved using the Implicit Characteristic Splitting scheme (ICS) as described in [20]. Applying the ICS scheme results in (Einstein notation)

$$\frac{\overline{\rho}^* - \overline{\rho}^n}{\Delta t} + \frac{\partial \overline{\rho}\,\widetilde{u}_i}{\partial x_i} - \overline{\rho}\,\frac{\partial \widetilde{u}_i}{\partial x_i} = 0, \tag{5}$$

$$\frac{\overline{\rho}\,\widetilde{u}_i^* - \overline{\rho}\,\widetilde{u}_i^n}{\Delta t} + \frac{\partial \overline{\rho}\,\widetilde{u}_i\widetilde{u}_j}{\partial x_j} - \overline{\rho}\,\widetilde{u}_i\frac{\partial \widetilde{u}_j}{\partial x_j} - \frac{\partial \overline{\tau}_{ij}+\tau_{t,ij}}{\partial x_j} = \overline{\rho}\,\widetilde{f}_i, \tag{6}$$

$$\frac{\overline{\rho}\,\widetilde{E}^* - \overline{\rho}\,\widetilde{E}^n}{\Delta t} + \frac{\partial \overline{\rho}\,\widetilde{u}_i\widetilde{E}}{\partial x_i} - \overline{\rho}\,\widetilde{E}\frac{\partial \widetilde{u}_i}{\partial x_i} - \frac{\partial \widetilde{u}_j\left(\overline{\tau}_{ij}+\tau_{t,ij}\right)}{\partial x_i} + \frac{\partial \overline{q}_i+q_{t,i}}{\partial x_i} = \overline{\rho}\,\widetilde{u}_i\widetilde{f}_i + \bar{S}_r, \tag{7}$$

$$\frac{\overline{\rho}\,\widetilde{Y}_\alpha^* - \overline{\rho}\,\widetilde{Y}_\alpha^n}{\Delta t} + \frac{\partial \overline{\rho}\,\widetilde{u}_i\widetilde{Y}_\alpha}{\partial x_i} - \overline{\rho}\,\widetilde{Y}_\alpha\frac{\partial \widetilde{u}_i}{\partial x_i} + \frac{\partial \overline{j}_{\alpha i}+j_{t,\alpha i}}{\partial x_i} = \bar{S}_\alpha \tag{8}$$

for the advective and (Einstein notation)

$$\frac{\overline{\rho}^{n+1} - \overline{\rho}^*}{\Delta t} - \frac{1}{\overline{c}^2}\frac{\overline{\delta p}}{\Delta t} = 0, \tag{9}$$

$$\frac{\overline{\rho}\,\widetilde{u}_i^{n+1} - \overline{\rho}\,\widetilde{u}_i^*}{\Delta t} - \frac{\widetilde{u}_i}{\overline{c}^2}\frac{\overline{\delta p}}{\Delta t} + \frac{\partial}{\partial x_i}\left(\frac{\overline{p}^* + \overline{p}^{n+1}}{2}\right) = 0, \tag{10}$$

$$\frac{\overline{\rho}\,\widetilde{E}^{n+1} - \overline{\rho}\,\widetilde{E}^*}{\Delta t} - \frac{\widetilde{E}}{\overline{c}^2}\frac{\overline{\delta p}}{\Delta t} + \frac{\partial}{\partial x_i}\left(\frac{\widetilde{u}_i\,\overline{p}^* + \widetilde{u}_i\,\overline{p}^{n+1}}{2}\right) = 0, \tag{11}$$

$$\frac{\overline{\rho}\,\widetilde{Y}_\alpha^{n+1} - \overline{\rho}\,\widetilde{Y}_\alpha^*}{\Delta t} - \frac{\widetilde{Y}_\alpha}{\overline{c}^2}\frac{\overline{\delta p}}{\Delta t} = 0 \tag{12}$$

for the acoustic subsystem. In Eqs. (5)-(12), c is the speed of sound, Δt denotes the discrete time step size whereas $(\cdot)^n$, $(\cdot)^*$, and $(\cdot)^{n+1}$ represent the current, intermediate, and next time levels. With $\delta p = p^{n+1} - p^*$ a pressure correction is introduced and a pressure correction equation given through (Einstein notation)

$$\frac{\partial^2}{\partial x_i x_i}\overline{\delta p} - \frac{\partial}{\partial x_i}\left(\frac{2\widetilde{u_i}}{\Delta t\,\overline{c}^2}\overline{\delta p}\right) - \frac{4}{\overline{c}^2\,\Delta t^2}\overline{\delta p} = -2\frac{\partial^2}{\partial x_i x_i}\vec{p}^* + \frac{4}{\Delta t}\left(\frac{\overline{\rho}^* + \overline{\rho}^n}{2}\frac{\partial \widetilde{u_i^n}}{\partial x_i}\right) \tag{13}$$

is derived (cf. [20]). Further, numeric dissipation is introduced into the acoustic step to stabilize the solution and maintain a monotonic scheme. The advective subsystem Eqs. (5)-(8) is discretized using a temporal second order implicit Crank Nicolson scheme. Application of an implicit instead of an explicit discretization increases the stability (which is especially beneficial for numerically stiff combustion problems) but leads to a nonlinear system of equations. With the introduction of a linearization for the unknown flux and source vectors and the application of the Newton Raphson scheme a fully implicit procedure for the advective subsystem is obtained. The pressure correction equation (Eq. (13)) is also discretized in a fully implicit manner. For the pressure correction variable δp, Dirichlet boundary conditions are applied at inflows and outflows whereas at walls von Neumann boundaries are used. Subsequent to solving the pressure correction equation the solution is advanced using the pressure correction δp in Eqs. (9)-(12). The scheme is implemented in the in-house code ThetaCOM [21] using a cell-vertex [22] approach where based on a primary grid a median-dual mesh is constructed. A detailed description of the method is given in [20].

III. Test case

A schematic drawing of the PRECCINSTA combustion device is given in Fig. 1. As indicated, the combustor is split up into several sections. At the most upstream point, air is supplied to the air plenum. The supply line is choked to enable a defined acoustic inflow condition. From there the air is guided into the swirler, where it mixes inside the swirler vanes in a jet in crossflow configuration with the fuel coming from the fuel plenum. In total, twelve swirler vanes and therefore twelve fuel ports with a diameter of $D = 1$ mm are used. The so called technically premixed air-fuel mixture is guided into the combustion chamber via a duct connecting both sections. In the center of this connecting duct the bluff body is located. As indicated in Fig. 1 the origin of the used coordinate system is located at the tip of the conical bluff body. The combustion chamber has a square cross section with a lateral length of $L = 85$ mm and a height of $H = 114$ mm. All four side walls of the combustion chamber are made of quartz glass windows providing optical access for measuring. The quartz glasses are held by metal corner posts which are mounted into the base plate. At the downstream end of the combustion chamber the converging outlet section is placed. Here, the rectangular cross section transitions into a circular cross section and the exhaust gases are leaving the device through the converging outlet's short exhaust pipe. All reference data are acquired under atmospheric conditions where air is used as oxidizer and pure methane is used as fuel. The chosen operational point of the burner has a thermal power of $P_{\text{th}} = 25$ kW at an equivalence ratio of $\phi = 0.7$. This results in a fuel mass flow of $\dot{m}_{\text{fuel}} = 30$ g/min with an air mass flow of $\dot{m}_{\text{air}} = 743$ g/min, considering air with a composition of $Y_{\text{O}_2} = 0.23$ and $Y_{\text{N}_2} = 0.77$. Here, Y_{O_2} and Y_{N_2} denote the mass fractions for Oxygen and Nitrogen, respectively.

IV. Numerical modeling

The reactive flow of the PRECCINSTA combustion device described in Sec. III is computed using the method described in Sec. II. Inflow and outflow boundaries are modeled using the Navier Stokes characteristic boundary conditions (NSCBC) approach of [23] as described in [20]. Here, the air inflow is assumed to be stiff, representing the chocked inflow of the test case. Likewise, the inflow for the fuel is also taken to be stiff. Here, the fuel plenum is included in the computational domain. In this way the stiff inflow for fuel is placed away from the injection holes at the swirler vanes. The mass flows for fuel and air are set according to the chosen operational point defined in Sec. III. Temperatures of the inflow streams are set to 320 K in accordance with the combustion chamber inflow temperature reported in the experiments [5]. For the outflow boundary a subsonic partially reflecting approach is applied where the reflection factor is defined by $K = \sigma_{\text{out}}(1 - Ma_{\text{out}})c/L_{\text{out}}$. In this context, K is the relaxation parameter at the outflow boundary whereas Ma_{out}, σ_{out}, and L_{out} are the case dependent Mach number, relaxation parameter, and characteristic length. Values for these parameters are summarized in Tab. 1. At the combustion chamber side walls as well as the combustion chamber base plate isothermal wall boundary conditions with a defined temperature profile

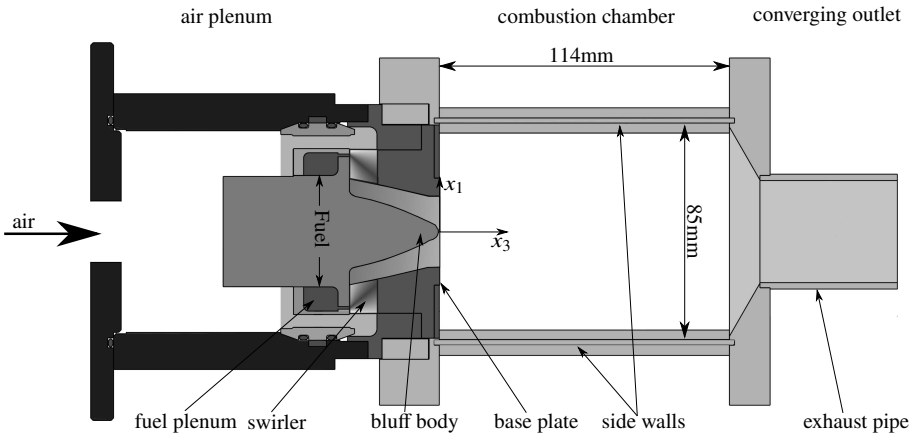

Fig. 1 Schematic drawing of the investigated combustion device.

L_{out} [m]	Ma_{out}	σ_{out}	p_{out} [Pa]
0.18	0.10	0.28	101325

Table 1 NSCBC parameters for the outflow boundary of the PRECCINSTA test case.

are prescribed. Remaining wall boundaries are assumed to be isothermal with a temperature of 320 K. The system of equations presented in Sec. II is in the Favre filtered form. The subgrid-scale stress tensor in Eq. (6) is closed using the wall-adapting local eddy-viscosity (WALE) model given in [24], where the WALE constant is set to $C_W = 0.1$. To close the subgrid-scale energy and species fluxes in Eqs. (7) and (8), a gradient diffusion approach is used relating the fluxes to the Favre filtered temperature and mass fraction gradients. The required turbulent diffusivities are calculated based on the eddy-viscosity and the turbulent Prandtl and Schmidt numbers. A constant timestep of $\Delta t = 0.1\mu$s is applied for all computations. In total, five different simulations are conducted where an overview is given in Tab. 2 with case one being the baseline. As provided in Tab. 2 the computations differ from case one either by the chosen domain, the used reaction mechanism, the selected combustion model, or the applied model parameters. In detail, case one and case two differ in the applied computational domain. For case one, domain A without an outlet plenum is used whereas for case two, a plenum is attached to the end of the short exhaust pipe downstream the converging outflow section. A cut through domain A and B is depicted in Fig. 2. As compared to domain A, domain B aims to diminish the influence of the NSCBC outflow boundary onto the solution by placing the NSCBC outflow far away from the exhaust pipe's exit. Both domains are discretized with a hybrid mesh consisting of about 5.1 million grid points for domain A and about 5.2 million grid points for domain B. To avoid backflow at the recessed outflow, an additional inflow is set at the upstream boundary of the added plenum for case two. This generates an axial coflow where a velocity of 15 m/s is applied. The combustion processes are modeled using a finite-rate chemistry approach where the chemical kinetics are described by either the DRM19 [25] for case one, two, four, and five or by a reduced variant of the DLR-Concise (DC1S29) [26] mechanism in case three. Considering the combustion model, except for

Case	Domain	Mechanism	Combustion model	Model parameter
case 1	A	DRM19	APDF	$Sc_t = Pr_t = 0.7$
case 2	**B**	DRM19	APDF	$Sc_t = Pr_t = 0.7$
case 3	A	**DC1S29**	APDF	$Sc_t = Pr_t = 0.7$
case 4	A	DRM19	**TF**	$Sc_t = Pr_t = 0.7$
case 5	A	DRM19	APDF	$\boldsymbol{Sc_t = Pr_t = 0.4}$

Table 2 Overview of the conducted compressible LES.

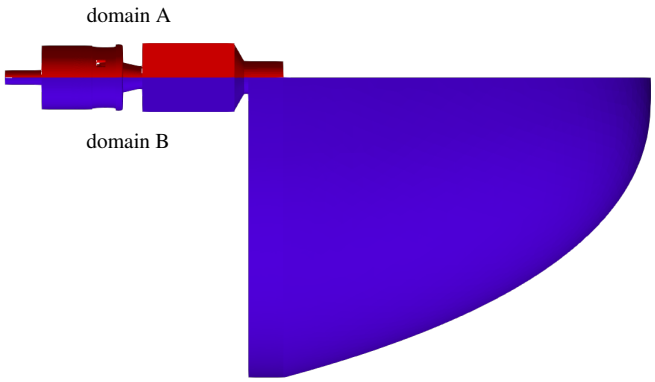

Fig. 2 Cut through the computational domain used for the compressible LES. Domain A (red) without a plenum for the atmosphere. Domain B (blue) with a plenum for the atmosphere.

case four, an assumed probability density function (APDF) [27, 28] model is used. Case four, applies the thickened flame (TF) model of [29] where the thickness factor is computed dynamically [30] based on the ratio of the local mesh size and the local thickness of a laminar premixed flame. Finally, the turbulent Schmidt and Prandtl numbers are set to $Sc_t = Pr_t = 0.7$ for all cases except case five where $Sc_t = Pr_t = 0.4$ is used.

V. Results

First, a general comparison of the computed results of the five considered cases is given to obtain an overview of the discrepancies induced by the different modeling approaches. This includes a comparison of the computed results against experimental reference data from [5, 11], also. Following, a more detailed investigation of the differences between the individual cases is given.

A. General comparison

Starting with the temporal averaged velocities, results for the computations along with data acquired from measurements are given in Fig. 3. The velocity profiles shown are extracted at two different heights inside the combustion chamber and plotted along the x_1-direction. In Fig. 3a and Fig. 3c, the averaged axial velocities at the heights $x_3 = 1.5\,\text{mm}$ and $x_3 = 35\,\text{mm}$ are given. For the same heights the averaged tangential velocities are plotted in Fig. 3b and Fig. 3d. Overall a very good agreement for the averaged axial velocity directly above the burner at $x_3 = 1.5\,\text{mm}$ is obtained for all cases in comparison with the experimental data. No significant differences exist between the computed results. Also for the tangential velocity at $x_3 = 1.5\,\text{mm}$ a good agreement with the experimental findings is obtained where the measured tangential velocity is slightly overestimated in the range of $-14\,\text{mm} < x_1 < -1\,\text{mm}$. In contrast, the slope at $x_1 = -15\,\text{mm}$ is matched well by the computed results. Small differences between the computed results are observable, leading to somewhat lower velocities for case four, resulting in a small increase in agreement of this case and the experimental tangential velocities in the vicinity of the burner. Further downstream at $x_3 = 35\,\text{mm}$ the comparison of the averaged axial velocity with the experimental data shows that the computed results are shifted towards the center by about 5 mm. An exception is case four, where the shift amounts to about 2.5 mm. Apart from this shift, the overall peak velocity of about $30\,\text{m/s}$ agrees well between the computational results and the experimental data. Considering the averaged tangential velocity at $x_3 = 35\,\text{mm}$ in Fig. 3d the pattern continues, where overall a good agreement with a slight velocity overestimation in the computed results is observed. Again, only case four somewhat deviates from the other computed results, showing marginally lower velocities. Overall, the changes introduced to the numerical model for cases one to five do not significantly influence the averaged velocity fields inside the combustion chamber. However, this is not the case for other important quantities such as the emerging pressure fluctuations inside the combustion chamber. In Tab. 3 an overview of the computational results for cases one to five together with the experimental data provided in [11] is given. For each case and the measurement the frequencies of the fundamental mode f_0 and the first harmonic f_1 are noted. Alongside the frequencies the overall sound pressure level (SPL) is given. The frequencies are extracted from the computed power spectral densities (PSD) based on the combustion chamber pressure time signal. Integrating the PSD leads to the SPL where the acoustical reference pressure of $p_a = 20\,\mu\text{Pa}$ is used for conversion to

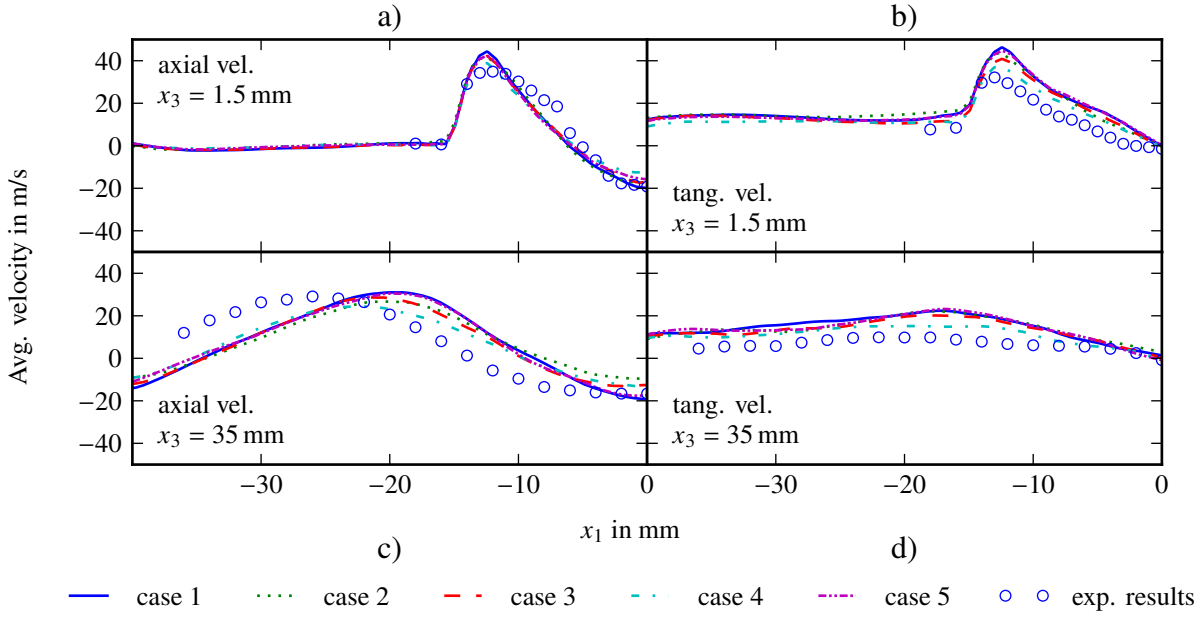

Fig. 3 Averaged velocities at different heights over the x_1-coordinate. a) averaged axial velocities at $x_3 = 1.5$ mm. b) averaged tangential velocities at $x_3 = 1.5$ mm. c) averaged axial velocities at $x_3 = 35$ mm. d) averaged tangential velocities at $x_3 = 35$ mm. Experimental results are from [5].

	case 1	case 2	case 3	case 4	case 5	exp. results
f_0 [Hz]	280	364	244	205	275	274
f_1 [Hz]	566	728	484	416	544	547
SPL [dB]	162.55	158.89	161.85	161.14	161.61	154.26

Table 3 Overview of the computed results as well as reference data from experiments (c.f. [11]) for the pressure fluctuations inside the combustion chamber. f_0 is the fundamental frequency and f_1 the first harmonic. Besides the frequencies the overall sound pressure level (SPL) is indicated.

decibel. As compared to the experiment, cases one and four obtain the best agreement in terms of frequencies f_0 and f_1. Case three and case four however, underestimate the frequencies obtained in the experiment considerably. In case two, the opposite is observed where with $f_0 = 364$ Hz the computed frequency obtained is significantly overestimates the measured frequency. The overall SPL follows a different trend. Here, the experimentally obtained SPL is overestimated by all computed results where an offset of about 8 dB is observed for the computational results of cases one, three, four, and five. The lowest computed SPL is obtained for case two only overestimating the experimentally obtained SPL by roughly 4 dB. The computed PSDs for the baseline case one alongside case two and four covering the lowest and highest computed frequencies are plotted in Fig. 4. Besides the computational results the PSD based on the experimental pressure time series is plotted. Considering case four, it is apparent that unlike to case one and case two the second peak at f_1 is much weaker. Also a second harmonic at roughly $3f_0$ is almost completely suppressed in case four. The overall qualitative trend however, is well recovered by the computed results as compared to the experiment. Next, the flame shapes and lift off heights between the simulated results are compared. For this reason the computed heat release is considered. In Fig. 5, contour plots of the normalized time averaged heat release are given for each case. To compare the overall flame shape and lift off height, the normalized line of sight integrated heat release inside the combustion chamber is plotted in the first row. Normalization is obtained by the maximal value of the line of sight integrated heat release over all cases. The second row shows the averaged heat release for each case inside the duct between the swirler and

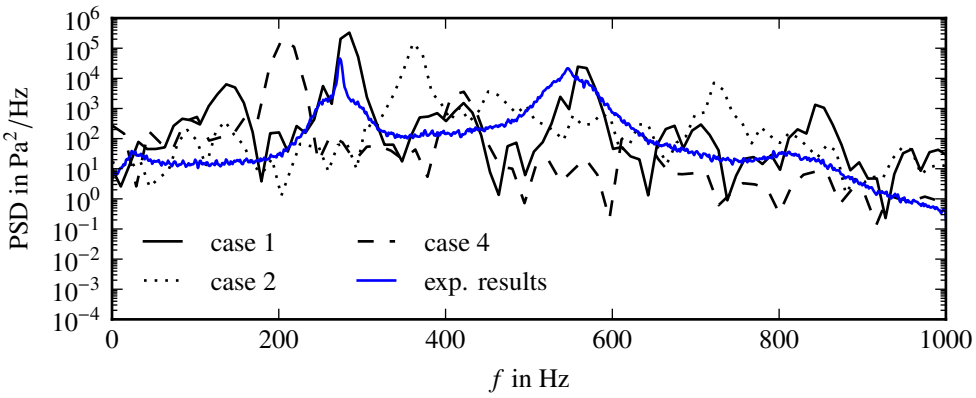

Fig. 4 Power spectral density of the pressure inside the combustion chamber for the cases one, two, and four as well as an experimental spectrum [11].

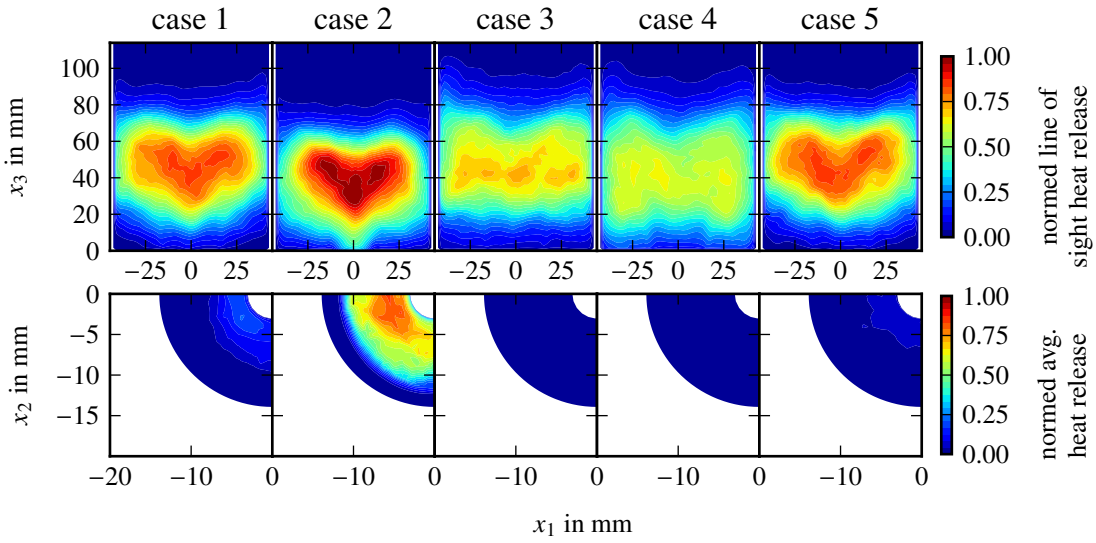

Fig. 5 Computed heat release for cases one to five. In the first row the normalized line of sight integrated heat release inside the combustion chamber is shown. In the second row the temporal averaged heat release in a sector of the duct between swirler and combustion chamber at $x_3 = -2.5$ mm is given.

the combustion chamber at $x_3 = -2.5$ mm. Here, only a sector for $-20\,\text{mm} \leq x_1 \leq 0\,\text{mm}$ and $-20\,\text{mm} \leq x_2 \leq 0\,\text{mm}$ is displayed where again, the maximal value over all cases is used for normalization. Comparing the flame shape by means of the line of sight integrated averaged heat release clear differences are apparent between the cases one to five. The characteristic shapes can be linked to the observations made in the combustion chamber pressure. Where case one and case five obtain similar frequencies considering the fundamental mode as well as the higher harmonics, they here also display similar characteristics in terms of flame shape, lift off height, and heat release intensity. Based on the line of sight integrated heat release, a lifted flame is obtained where the flame root is located at $x_3 = 12$ mm in both cases. In the vicinity of the flame root the intensity is highest towards $x_1 = 0$ mm and gets weaker moving closer to the combustion chamber side walls at a constant height from the base plate. Further downstream the regions of high intensity cover the whole cross section of the combustion chamber. Considering the averaged heat release inside the duct displayed in the second row of Fig. 5, only a low intensity is observed in the proximity of the conical bluff body for both cases. By analysing the temporal evolution of the computed heat release it is seen that such an averaged heat release

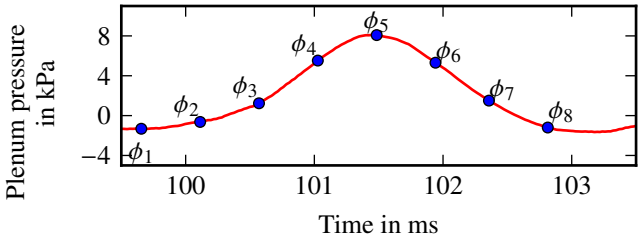

Fig. 6 Definition of the phases based on the pressure of the air plenum for one cycle.

inside the duct originates from a small number of flash back events. Different observations are made for cases three and four where the fundamental mode is found to show lower frequencies as compared to case one. Opposed to case one, no averaged heat release is detected in the duct between swirler and combustion chamber. Further, the flame shapes based on the line of sight integrated heat release are also considerably different. Where for case one the flame root extents towards the tip of the bluff body this behavior is not observed for cases three and four. Here, for case three an almost horizontal upstream bound is obtained for the line of sight integrated heat release whereas for case four the contours extend further upstream in the region near to the combustion chamber side walls as compared to the center. Analogous to the combustion chamber pressure, a different observation is made for case two. As compared to the other cases, case two exhibits the highest frequencies for the occurring pressure modes. By comparing the averaged heat release inside the duct in the second row of Fig. 5 case two also stands out. Here, it is apparent that the highest intensities in averaged heat release of all cases are found. Again, a temporal analysis of the heat release shows that these high values of averaged heat release originate from flash back events into the duct. Further, case two is the only case where significant heat release is obtained close to the tip of the bluff body at the combustion chamber entrance, indicating on average an attached flame. Overall, concerning the pressure mode as well as the heat release a strong influence of the model approach is obtained. Most notably are the influence of the outflow modeling, the chosen reaction mechanism modeling the chemical kinetics, as well as the applied combustion model. For the current setup, the influence of the model parameters, namely the turbulent Prandtl and Schmidt numbers, is negligible and not considered further. In the following a closer look is taken on the distinct influence of the modifications introduced to the numerical model.

B. Influence of the outflow modeling

Case one and two only differ in the modeling of the outflow boundary. For case one the NSCBC subsonic partially reflecting outflow boundary is directly located at the exit of the short exhaust pipe. In contrast, for case two the computational domain is extended downstream the exhaust pipe in order to move the NSCBC subsonic partially reflecting outflow boundary away from the chamber's outlet thus mitigating its influence on the combustion chamber's outlet modeling. As described in Sec. V.A, concerning the combustion chamber pressure modes and flame characteristic significant effects are observed. First of all, the flame switches from a lifted flame to an attached flame as indicated by the contour plots of the averaged heat release given in Fig. 5. This goes along with significantly higher frequencies for the pressure modes inside the combustion chamber as shown in Fig. 4. The differences in flame lift off height influences the temperatures directly at the entrance of the combustion chamber. This is seen in Fig. 7 where the averaged temperatures of cases one and two are compared with the experimental values acquired in [5]. In detail, the time averaged temperatures at a height of $x_3 = 6\,\text{mm}$ along the positive x_1-coordinate are plotted in Fig. 7a. At the same position the phase averaged temperatures for the experimental results of [5] are given in Fig. 7b together with the phase averaged temperatures for case one in Fig. 7c and case two in Fig. 7d. The phases are defined based on the pressure inside the air plenum as described in [5] and shown in Fig. 6. Regarding the temperature profiles given in Fig. 7a, the experiments conducted in [5] on average detect high temperatures of about 1610 K in proximity to the tip of the bluff body at $x_1 = 0\,\text{mm}$. With increasing distance from the center, the average temperature drops monotonically up to $x_1 \leq 14\,\text{mm}$ where it reaches a minimal value of about 370 K. In the range of $14\,\text{mm} < x_1 \leq 21\,\text{mm}$ the average temperature rises again and reaches a plateau with a value of about 1560 K. This is in contrast to the computed solutions where the qualitative trend is somewhat reproduced but does fail to match the quantitative values. For case one, this

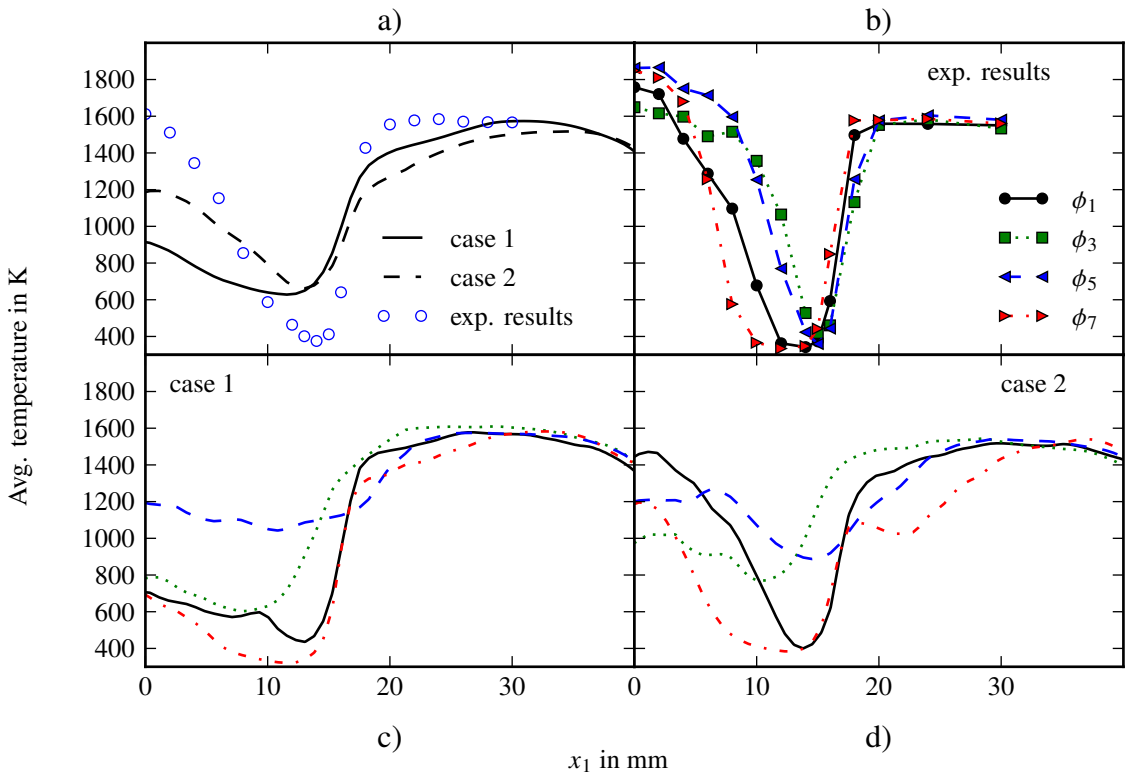

Fig. 7 Averaged temperature at $x_3 = 6$ mm. a) time average of cases one and two as well as experimental values from [5]. b) phase averaged measured temperatures of [5]. c) phase averaged temperatures of case one. d) phase averaged temperatures of case two.

results in a temperature downstream the tip of the bluff body of about 910 K and a minimal temperature of about 640 K at $x_1 = 12$ mm. With increasing values for x_1 the averaged temperature rises analogously to the experiments but no clear plateau region is obtained. Similar to the averaged line of sight integrated heat release (c.f. Fig. 5) case two behaves differently. In proximity to the tip of the bluff body at $x_1 = 0$ mm much higher averaged temperatures of about 1185 K as compared to case one are computed displaying a better agreement with the experimental values. With increasing distance to the tip of the bluff body in x_1-direction the temperatures decrease until $x_1 = 13$ mm where temperatures comparable to case one are obtained. The ensuing rise in temperature for increasing x_1 is smaller leading to a better agreement of case one instead of case two compared to the experimental values in this region. Considering the phase averaged results further peculiarities between the experimental and the computed results for case one and two are observed. First of all, in the experiments of [5] displayed in Fig. 7b at $x_1 = 0$ mm the temperature for the different phases remain at high values indicating a anchoring flame over the whole cycle. Also the minimal temperature stays roughly at the same value. Further, the steep increase in temperature as well as the temperature of the plateau are at the same location respectively at the same value between the phases. The main differences between the phases are obtained in the regions where the temperature decreases ($0\,\text{mm} < x_1 \leq 13\,\text{mm}$). This results in differences in the spatial extent of the low temperature regions throughout the cycle. Comparing the experimental phase averaged temperatures to the computed results an overall better agreement is obtained for case two given in Fig. 7d than for case one plotted in Fig. 7c. At $x_1 = 0$ mm the temperatures are high for case two throughout the whole cycle whereas for case one only phase ϕ_5 obtains comparable high temperatures. Considering the development of the phase averaged temperatures for case two, only phases ϕ_1 and ϕ_7 are in qualitative agreement with the experimental findings. At least for phase ϕ_7, this qualitative agreement is restricted by an interruption of the temperature increase at $x_1 = 17$ mm.

Now, a closer look is taken on the computed pressure fluctuations of case one and two. The pressure fluctuations are calculated being the standard deviation of the filtered pressure. In Fig. 8, contour plots in the x_1, x_3-plane at $x_2 = 0$ m

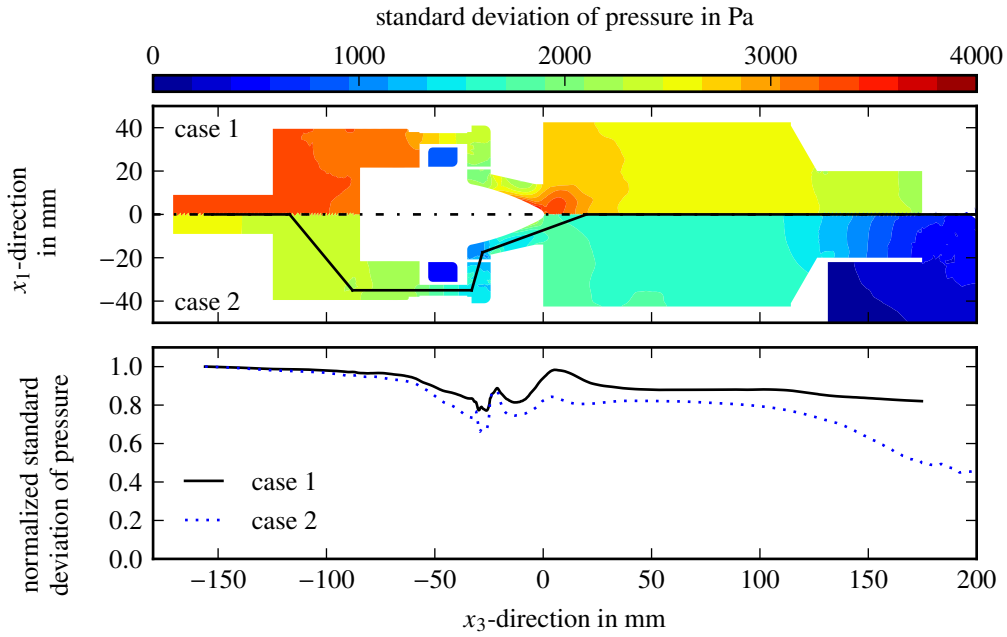

Fig. 8 Comparison of the standard deviation of pressure for case one and case two. The first row shows contour plots of the standard deviation in the x_1, x_3-plane at $x_2 = 0$ m for case one (top half) and case two (lower half). The second row gives the normalized standard deviation extracted along the path indicated in the contour plots of the first row.

for the standard deviation of pressure for cases one and two are given. The contour plot of the standard deviation of the pressure is split up along the centreline displaying case one at $x_1 > 0$ mm and case two at $x_1 < 0$ mm. Alongside the contour plots in the first row, a diagram is provided in the second row of Fig. 8. This diagram displays the normalized standard deviation of pressure extracted along the path indicated in the contour plots above. The maximal value which is also the most upstream extracted point, is used for normalization of the standard deviation of pressure in the line diagram. Considering the normalized standard deviation of pressure extracted along the indicated line it is apparent that higher values are obtained for case one as compared to case two. This behavior starts at $x_3 > -50$ mm and persists up to the outflow boundary. Towards the downstream end of the combustion chamber, for $x_3 > 100$ mm the discrepancies between case one and case two are getting larger. A lower standard deviation of pressure at the outflow may relate to a higher reflection coefficient of the outflow boundary. This assumption is based on the consideration, that in the limit of a constant pressure, a pressure node with a vanishing standard deviation of pressure would be imposed at the outflow. Such an outflow is associated with a reflecting boundary where the magnitude of the reflection coefficient becomes one. Using a simplified one dimensional series of ducts model it can be shown that for the considered case, a higher magnitude of the reflection factor at the outflow is associated with a higher fundamental mode frequency f_0. The simplified model follows the approach described in [31, 32] for longitudinal modes in series of constant cross section ducts. For this reason the PRECCINSTA combustion device is split up into seven regions of constant cross section as shown in Fig. 9. Each region is associated with a cross section area S and a length a. The regions are related to each other by means of six interfaces denoted by I. Further, averaged values for the speed of sound and the density are required in each section. These values are extracted from the computed LES results. All required model parameters are given in Tab. 4. According to [31, 32] the acoustic field in region n can be described by

$$p'_n(x,t) = \left(A_n^+ e^{\mathrm{i}k_n(x-x_n)} + A_n^- e^{\mathrm{i}k_n(x-x_n)} \right) e^{-\mathrm{i}\omega t} \tag{14}$$

and

$$u'_n(x,t) = \left(\frac{A_n^+}{\rho_n c_n} e^{\mathrm{i}k_n(x-x_n)} + \frac{A_n^-}{\rho_n c_n} e^{\mathrm{i}k_n(x-x_n)} \right) e^{-\mathrm{i}\omega t}, \tag{15}$$

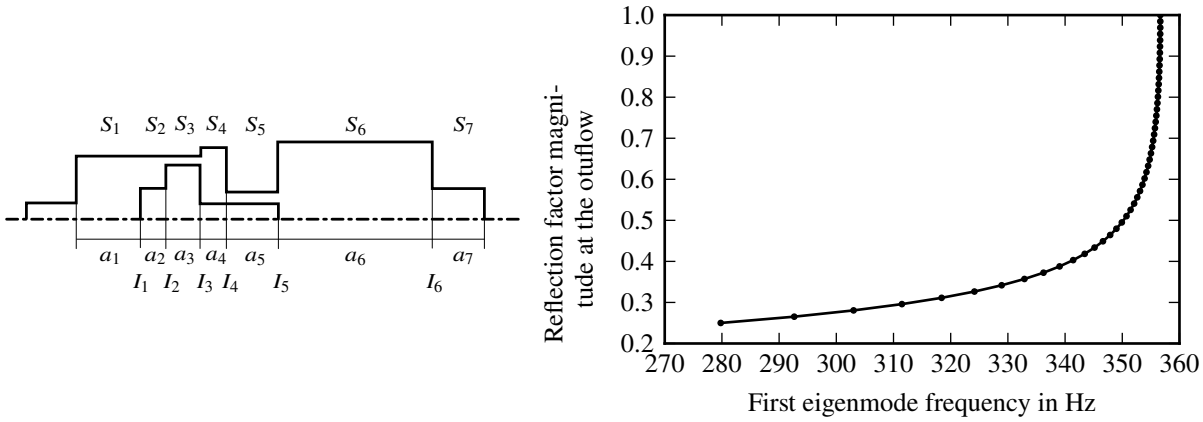

a) b)

Fig. 9 Eigenmode analysis for the PRECCINSTA burner based on a one dimensional series of ducts model. a) definition of the duct segments where S denotes the section, a the section length, and I the section interfaces. b) resulting frequencies for the first Eigenmode over the magnitude of the reflection factor.

Section number n	1	2	3	4	5	6	7
a_n in mm	40.00	28.00	22.00	10.50	25.00	120.00	54.00
S_n in mm^2	4901.67	3516.23	1200.87	5089.38	607.71	7225.00	1256.64
c_n in m/s	360.00	360.00	360.00	360.00	360.00	820.00	820.00
ρ_n in kg/m^3	1.10	1.10	1.10	1.10	1.10	0.20	0.20

Table 4 Model parameters for the one dimensional acoustic model. n is the number of each section, a_n is the length of section n, S_n the cross section area, c_n the speed of sound, and ρ_n the averaged density.

assuming the simplifications for linear acoustic hold. Here, p' and u' denote the acoustic pressure and velocity while $\mathrm{i} = \sqrt{-1}$ is the imaginary unit. Further, A is the acoustic amplitude and the superscripts $(\cdot)^+$ and $(\cdot)^-$ denote left and right moving waves with respect to the spatial coordinate x. Additionally, $k = \omega/c$ is the wave number and $\omega = 2\pi f$ the angular frequency of the frequency f. For each segment, the amplitudes of adjacent regions are related by

$$\begin{pmatrix} A^+_{n+1} \\ A^-_{n+1} \end{pmatrix} = \underbrace{\frac{1}{2}\begin{pmatrix} e^{\mathrm{i}k_n a_n}(1+\Gamma_n) & e^{-\mathrm{i}k_n a_n}(1-\Gamma_n) \\ e^{\mathrm{i}k_n a_n}(1-\Gamma_n) & e^{-\mathrm{i}k_n a_n}(1+\Gamma_n) \end{pmatrix}}_{T_n} \begin{pmatrix} A^+_n \\ A^-_n \end{pmatrix}, \quad \text{with} \quad \Gamma_n = \frac{\rho_{n+1} c_{n+1} S_n}{\rho_n c_n S_{n+1}}, \tag{16}$$

demanding that pressure and acoustic flow rate are constant across the interface. Based on the transfer matrices T_n a global matrix G can be constructed relating the amplitudes of the first to the last region through

$$\begin{pmatrix} A^+_7 \\ A^-_7 \end{pmatrix} = G \begin{pmatrix} A^+_1 \\ A^-_1 \end{pmatrix}, \quad \text{with} \quad G = \prod_{n=1}^{6} T_n. \tag{17}$$

The system is closed through the boundary conditions

$$\frac{A^+_1}{A^-_1} = R_I \quad \text{and} \quad \frac{A^+_7}{A^-_7} e^{2\mathrm{i}k_7 a_7} = R_O,$$

where R_I and R_O are the reflection coefficients for the inflow and outflow. Solving the linear system of Eq. (17) using the boundary conditions leads to

$$0 = \frac{R_I G_{1,1} + G_{1,2}}{R_I G_{2,1} + G_{2,2}} e^{2\mathrm{i}k_7 a_7} - R_O, \tag{18}$$

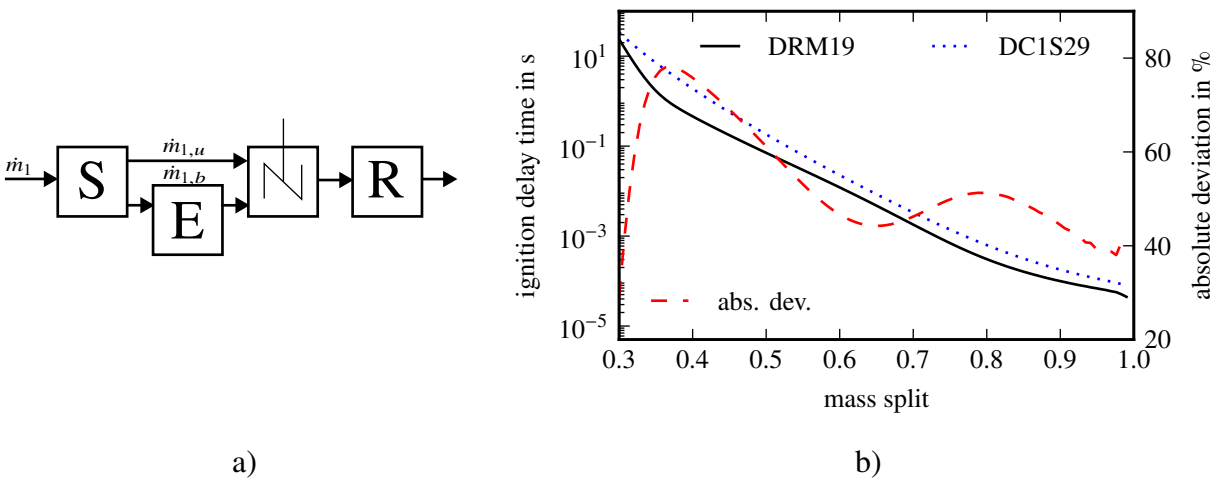

a) b)

Fig. 10 Comparison of the applied reaction mechanisms. a) flowchart of the calculation procedure. $\dot{m}_1$ is the total stream entering the system. $\dot{m}_{1,u}$ and $\dot{m}_{1,b}$ are the unburnt and burnt streams. b) results for the ignition delay time over the mass split for the applied reaction mechanisms.

where the complex roots are the longitudinal Eigenmodes of the system. For the case considered here, it is assumed that the inflow is a velocity node expressed by $R_I = 1$. In contrast, the outflow is assumed to be terminated by a large vessel with a varying reflection coefficient R_O. In Fig. 9b the frequency of the first Eigenmode calculated by the one dimensional model is plotted over the magnitude of the reflection factor at the outflow. Considering the simple approach without acoustic source, the computed Eigenmodes by the one dimensional model are in a good agreement with the frequencies obtained by the LES and experiments. Depending on the magnitude of the reflection factor at the outflow, the first Eigenmode takes values between 280 Hz $\leq f_0 \leq$ 357 Hz. This reveals a strong influence of the outflow modeling on the frequency of the first Eigenmode of the system. The increase in frequency of the first Eigenmode with an increased reflection factor magnitude for the one dimensional series of ducts model supports the assumption that the shift in frequency for the LES is related to a higher reflection factor for case two as compared to case one. Another interesting observation is that a considerable shift in first Eigenmode frequency is only obtained for small reflection factor magnitudes of about $|R_O| \leq 0.5$. For $|R_O| > 0.5$ however, the differences in frequency for the first Eigenmode remain small. Referring to the measured frequency for the first pressure mode in the experiments, and based on the findings of the one dimensional model, the first Eigenmode frequency is associated with a small reflection factor magnitude at the outflow of about $|R_O| = 0.26$. However, this may only serve as an estimate, as the influence of the combustion processes is neglected.

C. Influence of the reaction mechanism and closure model for the filtered chemical source term

The difference between case one and three is the applied reaction mechanism modeling the chemical kinetics. For case one the DRM19 [25] reaction mechanism is applied whereas for case three the DC1S29 [26] reaction mechanism is utilized. As described in Sec. V.A the choice of the reaction mechanism mainly influences the averaged heat release (c.f. Fig. 5) as well as the frequencies of the occurring pressure modes (c.f. Tab. 3). The effect regarding the averaged velocities is negligible (c.f. Fig. 3). However, as shown in [10] during each cycle, depending on the current phase, the flame is either igniting, burning, fading, or almost extinguished. For this reason, the ignition delay time computed from the reaction mechanism might be a crucial factor for the overall behaviour of the computed solution. Further, the reignition during the cycles is dominated by the mixing of the entering cold, reactants with the hot products still present in the combustion chamber. This mixing of fresh and burnt gases is modeled separately to investigate the ignition delay of the two reaction mechanisms. For this reason a reactor network model is build using the software Cantera [33]. The set up of the model is schematically drawn in Fig. 10a. For the model it is assumed that the entering stream $\dot{m}_1$ is set to the combustion chamber entrance conditions. This corresponds to an equivalence ratio of 0.7, at ambient pressure for a temperature of 320 K. The stream $\dot{m}_1$ is split up depending on the mass split factor f_s into the streams $\dot{m}_{1,u} = (1 - f_s)\dot{m}_1$ and $\dot{m}_{1,b} = f_s\dot{m}_1$ indicated in the flow chart by the symbol S. Here, $\dot{m}_{1,u}$ is the stream of the unburnt, cold reactants which is directly conducted into the mixer. The burnt, hot products are denoted by $\dot{m}_{1,b}$ and are

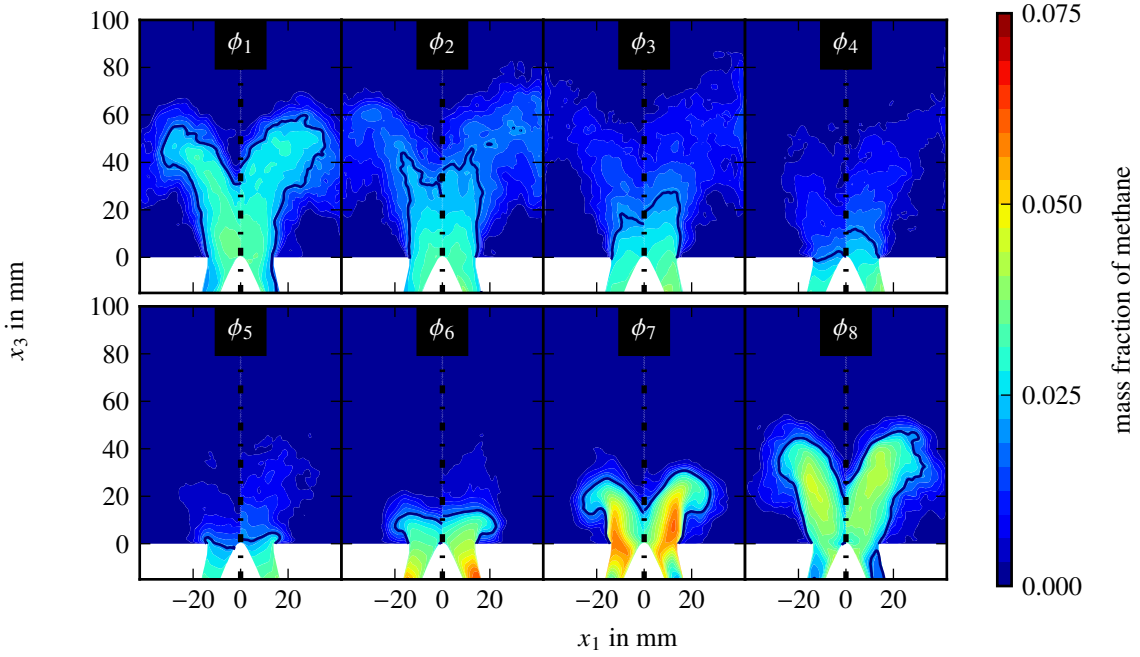

Fig. 11 Methane mass fractions in the x_1, x_3-plane at $x_2 = 0$ m for phases ϕ_1 to ϕ_8. For each phase, the contour plots show case one on the left side and case three on the right side. The drawn contour line in each plot is associated with the CH_4-mass fraction of 0.02.

brought into chemical equilibrium prior to being mixed with the cold reactants $\dot{m}_{1,u}$. In the flow chart the computation of the chemical equilibrium is denoted by E where isobaric, adiabatic conditions are assumed. For different mass split factors f_s, the ignition delay time is computed using a constant pressure batch reactor. In Fig. 10b the resulting ignition delay time is plotted over the mass split factor f_s for both reaction mechanisms. Comparing the results, it is obvious that the computed ignition delay time between the reaction mechanisms differs strongly. For the considered range in mass split factor f_s the DRM19 reaction mechanism obtains lower ignition delay times as the DC1S29 reaction mechanism. Alongside the values for the ignition delay time, Fig. 10b also gives the absolute deviation between both reaction mechanisms in percent. It is seen, that the deviation of the two reaction mechanisms is between 40 % up to almost 80 % whereas the deviation grows with low mass split factors f_s i.e. with decreasing initial temperature. The differences in ignition delay may explain the disparities observed in the line of sight integrated heat release shown in Fig. 5 for cases one and three. In contrast to case one, for case three, due to the delayed ignition, the reactants are able to penetrate further into the combustion chamber prior to being consumed by the combustion processes. This is illustrated by Fig. 11 where contour plots of the CH_4-mass fraction are given for both cases. In detail, Fig. 11 shows the averaged CH_4-mass fraction of the eight phases as defined by [5] and indicated in Fig. 6. For each phase, the contours are extracted in the x_1, x_3-plane at $x_2 = 0$ m, where separated by the dashed line, on the left side case one and on the right side case three is given. Further, the contour line for the CH_4-mass fraction of 0.02 is drawn. It is seen, that in general the CH_4 penetrates further into the combustion chamber for case three. Moreover, prior to reignition which starts in phase ϕ_2 it is also broader distributed in the combustion chamber as compared to case one. These differences may contribute to the increased lift off height obtained for case three as compared to case one.

A large impact in terms of heat release and occurring pressure modes is also observed for the choice of combustion model. In this particular case, the application of the thickened flame model for case four instead of the APDF model as in case one leads to a much lower pressure mode frequency and a more detached and broader averaged flame zone. Considering the averaged velocities in Fig. 3, again, only case four shows small deviations as compared to the remaining cases. An assumption could be that the combustion model chosen in case four reduces the dynamic motion of the flame as a result to the artificially thickened flame. Assuming that a reduced dynamic motion influence the processes of

reignition, burnout, and extinction similar mechanisms as observed for the differences in reaction mechanisms could lead to the observed differences for the obtained pressure mode. However, the origin remains speculative and requires more investigation by means of a detailed comparison of the applied combustion models which is out of scope of the present work.

VI. Summary and conclusion

A considerable influence of the numerical modeling approach for the investigated operational point of the PRECCINSTA combustor is observed. The most significant impact is caused by the outflow modeling where on average either an attached or detached flame is found. Nevertheless, the choice of the reaction mechanism and the choice of the combustion model also has a great influence on the flame as well as the frequency of the pressure mode. The impact of the turbulent Schmidt and Prandtl numbers is found to be insignificant for the considered parameters and ranges. In general, it is observed that higher frequencies of the fundamental pressure mode coincide with an attachment of the flame whereas a lifted flame is obtained for lower frequencies. Further, a negligible influence on the velocity fields is found. Based on the computed results for case one and case two in conjunction with the one dimensional series of ducts model, the significant influence of the outflow modeling is demonstrated. It is found, that the reflection coefficient largely influences the Eigenfrequency of the system. The differences in Eigenfrequencies in respect to the reflection coefficient are used to explain the differences in the computed frequencies of the first pressure mode for the cases one and two. Additionally, these findings may also give a possible explanation for the large spread of pressure mode frequencies found in literature. Further, a closer look is taken on the influence of the reaction mechanism. Again, this is done by means of a simplified model approach. In this way, it is found that the considered reaction mechanisms differ in ignition delay time. Based on these disparities an explanation for the obtained differences between cases one and three is derived. However, it has to be noted that the obtained differences between cases one and three cannot solely be explained by the differences in ignition delay time as further discrepancies between the reaction mechanisms may exist.

Acknowledgments

The authors gratefully acknowledge the scientific support and HPC resources provided by the German Aerospace Center (DLR). The HPC system CARA is partially funded by "Saxon State Ministry for Economic Affairs, Labour and Transport" and "Federal Ministry for Economic Affairs and Climate Action". The HPC system CARO is partially funded by "Ministry of Science and Culture of Lower Saxony" and "Federal Ministry for Economic Affairs and Climate Action".

References

[1] Dowling, A. P., and Hubbard, S., "Instability in Lean Premixed Combustors," *Proceedings of the Institution of Mechanical Engineers, Part A: Journal of Power and Energy Volume 214, Issue 4*, 2000, pp. 317–332. doi:10.1243/0957650001537903.

[2] Datta, A., Gupta, S., Chterev, I., Boxx, I., and Hemchandra, S., "Impact of Hydrogen Addition on the Thermoacoustic Instability and Precessing Vortex Core Dynamics in a CH4/H2/Air Technically Premixed Combustor," *Journal of Engineering for Gas Turbines and Power*, Vol. 144, No. 2, 2021, p. 021013. doi:10.1115/1.4052202.

[3] Weigand, P., Duan, X. R., Meier, W., Meier, U., Aigner, M., and Bérat, C., "Experimental Investigations of an Oscillating Lean Premixed CH_4/Air Swirl Flame in a Gas Turbine Model Combustor," *Proceedings of the European Combustion Meeting 2005*, 2005.

[4] Weigand, P., Meier, W., Duan, X., and Aigner, M., "Laser-Based Investigations of Thermoacoustic Instabilities in a Lean Premixed Gas Turbine Model Combustor," *Journal of Engineering for Gas Turbines and Power*, Vol. 129, No. 3, 2006, pp. 664–671. doi:10.1115/1.2718224.

[5] Meier, W., Weigand, P., Duan, X. R., and Giezendanner-Thoben, R., "Detailed Characterization of the Dynamics of Thermoacoustic Pulsation in a Lean Premixed Swirl Flame," *Combustion and Flame*, Vol. 150, No. 1, 2007, pp. 2–26. doi:10.1016/j.combustflame.2007.04.002.

[6] Arndt, C., Steinberg, A. M., Boxx, I. G., Meier, W., Aigner, M., and Carter, C. D., "Flow-Field and Flame Dynamics of a Gas Turbine Model Combustor during Transition between Thermo-Acoustically Stable and Unstable States," *Proceedings of the ASME Turbo Expo 2010: Power of Land, Sea and Air*, 2010.

[7] Boxx, I., Arndt, C. M., Carter, C. D., and Meier, W., "High-Speed Laser Diagnostics for the Study of Flame Dynamics in a Lean Premixed Gas Turbine Model Combustor," *Experiments in Fluids*, Vol. 52, 2012, pp. 555–567. doi:10.1007/s00348-010-1022-x.

[8] Steinberg, A., Arndt, C., and Meier, W., "Parametric Study of Vortex Structures and their Dynamics in Swirl-Stabilized Combustion," *Proceedings of the Combustion Institute*, Vol. 34, No. 2, 2013, pp. 3117–3125. doi:10.1016/j.proci.2012.05.015.

[9] Oberleithner, K., Stöhr, M., Im, S. H., Arndt, C. M., and Steinberg, A. M., "Formation and Flame-Induced Suppression of the Precessing Vortex Core in a Swirl Combustor: Experiments and Linear Stability Analysis," *Combustion and Flame*, Vol. 162, No. 8, 2015, pp. 3100–3114. doi:10.1016/j.combustflame.2015.02.015.

[10] Pries, M., Fiolitakis, A., Hadef, R., and Gerlinger, P., "Numerical and Experimental Investigation of Self Excited Thermoacoustic Instabilities in a Lean, Partially Premixed Swirl Flame," *AIAA SCITECH 2024 Forum*, 2024. doi:10.2514/6.2024-0592, No.: AIAA-2024-0592.

[11] Lourier, J.-M., Stöhr, M., Noll, B., Werner, S., and Fiolitakis, A., "Scale Adaptive Simulation of a thermoacoustic instability in a partially premixed lean swirl combustor," *Combustion and Flame*, Vol. 183, 2017, pp. 343–357. doi:10.1016/j.combustflame.2017.02.024.

[12] Franzelli, B., Riber, E., Gicquel, L. Y. M., and Poinsot, T., "Large Eddy Simulation of Combustion Instabilities in a Lean Partially Premixed Swirled Flame," *Combustion and Flame*, Vol. 159, No. 2, 2012, pp. 621–637. doi:10.1016/j.combustflame.2011.08.004.

[13] Lourier, J.-M., Noll, B., and Aigner, M., "Extension of a Compressible Pressure-Based Solver for Reacting Flows," *19th AIAA/CEAS Aeroacoustics Conference*, 2013. doi:10.2514/6.2013-2101, No.: AIAA-2013-2101.

[14] Lourier, J.-M., Noll, B., and Aigner, M., "Large Eddy Simulaiton of a Thermoacoustic Instability within a Swirl-Stabilzed Burner using Impedance Boundary Conditions," *Proceedings of ASME Turbo Expo 2014: Turbine Technical Conference and Exposition*, 2014. doi:0.1115/GT2014-26200, No.: GT2014-26200.

[15] Lourier, J.-M., Eberle, C., Noll, B., and Aigner, M., "Influence of Turbulence-Chemistry Interaction modeling on the Structure and the Stability of a Swirl-Stabilized Flame," *Proceedings of ASME Turbo Expo 2015: Turbine Technical Conference and Exposition*, 2015. doi:10.1115/GT2015-43174, No.: GT2015-43174.

[16] Fredrich, D., Jones, W. P., and Marquis, A. J., "A Combined Oscillation Cycle Involving Self-Excited Thermo-Acoustic and Hydrodynamic Instability Mechanisms," *Physics of Fluids*, Vol. 33, No. 8, 2021, p. 085122. doi:10.1063/5.0057521.

[17] Fredrich, D., Jones, W. P., and Marquis, A. J., "Thermo-acoustic Instabilities in the PRECCINSTA Combustor Investigated Using a Compressible LES-PDF Approach," *Flow, Turbulence and Combustion*, Vol. 106, 2021, pp. 1399–1415. doi:10.1007/s10494-020-00177-3.

[18] Zhao, S., Bhairapurada, K., Tayyab, M., Mercier, R., and Boivin, P., "Lattice-Boltzmann Modeling of the Quiet and Unstable PRECCINSTA Burner Modes," *Computers & Fluids*, Vol. 260, 2023, p. 105898. doi:10.1016/j.compfluid.2023.105898.

[19] Gövert, S., Lipkowicz, J. T., and Janus, B., "Compressible Large Eddy Simulations of Thermoacoustic Instabilities in the PRECCINSTA Combustor using Flamelet Generated Manifolds with Dynamic Thickened Flame Model," *Proceedings of the ASME Turbo Expo 2023*, 2023. doi:N/A, No.: GT2023-103438.

[20] Pries, M., Fiolitakis, A., and Gerlinger, P., "An Implicit Splitting Scheme with Characteristic Boundary Conditions for Compressible Reactive Flows on Unstructured Grids," *Journal of Computational and Applied Mathematics*, Vol. 437, 2024, p. 115446. doi:10.1016/j.cam.2023.115446.

[21] Setzwein, F., Ess, P., and Gerlinger, P., "An Implicit High-Order k-Exact Finite-Volume Approach on Vertex-Centered Unstructured Grids for Incompressible Flows," *Journal of Computational Physics*, Vol. 446, 2021, p. 110629. doi:10.1016/j.jcp.2021.110629.

[22] Barth, T., and Jespersen, D., "The Design and Application of Upwind Schemes on Unstructured Meshes," *27th Aerospace Sciences Meeting*, 1989. doi:10.2514/6.1989-366.

[23] Poinsot, T., and Lele, S., "Boundary Conditions for Direct Simulations of Compressible Viscous Flows," *Journal of Computational Physics*, Vol. 101, No. 1, 1992, pp. 104–129. doi:10.1016/0021-9991(92)90046-2.

[24] Nicoud, F., and Ducros, F., "Subgrid-Scale Stress Modelling Based on the Square of the Velocity Gradient Tensor," *Flow, Turbulence and Combustion*, Vol. 62, 1999, pp. 183–200. doi:10.1023/A:1009995426001.

[25] Kazakov, A., and Frenklach, M., "Reduced Reaction Set Based on GRI-Mech 1.2," , 2023. URL `http://www.me.berkeley.edu/drm/`, accessed: 2023-05-18.

[26] Kathrotia, T., Oßwald, P., Naumann, C., Richter, S., and Köhler, M., "Combustion kinetics of Alternative Jet Fuels, Part-II: Reaction Model for Fuel Surrogate," *Fuel*, Vol. 302, 2021, p. 120736.

[27] Gerlinger, P., Möbus, H., and Brüggemann, D., "An Implicit Multigrid Method for Turbulent Combustion," *Journal of Computational Physics*, Vol. 167, No. 2, 2001, pp. 247–276. doi:10.1006/jcph.2000.6671.

[28] Gerlinger, P., "Investigation of an Assumed PDF Approach for Finite-Rate Chemistry," *Combustion Science and Technology*, Vol. 175, 2003, pp. 841–872.

[29] Colin, O., Ducros, F., Veynante, D., and Poinsot, T., "A thickened Flame Model for Large Eddy Simulations of Turbulent Premixed Combustion," *Physics of Fluids*, Vol. 12, 2000, pp. 1843–1863.

[30] Charlette, F., Meneveau, C., and Veynante, D., "A Power-Law Flame Wrinkling Model for LES of Premixed Turbulent Combustion Part I: Non-Dynamic Formulation and Initial Tests," *Combustion and Flame*, Vol. 131, 2002, pp. 159–180.

[31] Poinsot., T. J., Trouve, A. C., Veynante, D. P., Candel, S. M., and Esposito, E. J., "Vortex-driven Acoustically Coupled Combustion Instabilities," *Journal of Fluid Mechanics*, Vol. 177, 1987, p. 265–292. doi:10.1017/S0022112087000958.

[32] Poinsot, T., and Veynante, D., *Theoretical and Numerical Combustion*, Edwards, 2005.

[33] Goodwin, D. G., Moffat, H. K., Schoegl, I., Speth, R. L., and Weber, B. W., "Cantera: An Object-oriented Software Toolkit for Chemical Kinetics, Thermodynamics, and Transport Processes," `https://www.cantera.org`, 2023. doi: 10.5281/zenodo.8137090, version 3.0.0.